

Modeling and performance analysis of forward and pressure-retarded osmosis

Hisham Ettouney^{a,*}, Khalida Al-Hajri^b

^aDepartment of Chemical Engineering, College of Engineering and Petroleum, Kuwait University, Kuwait, Tel. 0096566024661; email: ettouney@hotmail.com

^bDepartment of Mechanical Engineering, College of Engineering and Petroleum, Kuwait University, Kuwait, email: engk2@hotmail.com

Received 27 September 2018; Accepted 2 March 2019

ABSTRACT

This study simulates the performance of forward osmosis and pressure-retarded osmosis by the solution diffusion (SD) and the Spiegler–Kedem (SK) models in either complete mixing (CM) or plug flow (PF) configuration. The analysis considers the operating modes of placing the active side of the membrane facing the feed solution or the draw solution. This affects the magnitude of the concentration polarization on solute transport, which may occur inside the membrane support layer or in the bulk of the feed/draw solutions. The simulations illustrate the differences between these models and modes of operation on various important system parameters such as the membrane area, concentration and pressure of draw solution, flow rates of feed and draw solutions, recovery ratio, and power density. The results indicate that the placement of the active membrane layer facing the feed solution should only be considered for feed solutions containing a high concentration of particulate matter or fouling material. This is because operating with the active layer facing the draw solution provides better performance. Deviations in the predictions of the system characteristics by the SD model against the SK model are below 25%. Similarly, simulation of the spiral wound system by the CM model yields results within 15% of those predicted by the PF model.

Keywords: Desalination; Forward osmosis; Pressure-retarded osmosis; Complete mixing; Plug flow; Concentration polarization

1. Introduction

The forward osmosis (FO) process relies on using selective membranes between a high salinity draw solution and a lower salinity feed solution. The difference in salinity produces an osmotic pressure gradient that drives pure water from the feed side to the draw solution. The selection of an efficient draw solution requires using compounds that generate a high osmotic pressure, low cost, non-corrosive, and non-toxic, while not causing fouling or scaling [1,2]. Examples include sodium chloride, ammonium bicarbonate, and magnesium chloride [3]. More recently, Yang et al. [4] proposed using polyacrylic acid sodium salt that generates high water flux and low reverse salt flux. In addition, water recovery from the draw solution was

achieved by pH adjustment to yield the precipitation of the salt; subsequently, a micro filter is used to recover pure water from the water/precipitate mix.

In FO, the transmembrane pressure difference between the feed and draw solutions is equal to the osmotic pressure. However, the permeation of water from the feed to the draw solution results in the increase in the draw solution pressure. This condition is known as pressure-retarded osmosis (PRO), where the net transmembrane pressure is less than the osmotic pressure. The pressure-retard condition and water permeation from the feed side to the draw side continues provided that the transmembrane pressure difference between the feed and draw sides remains higher than zero. As the pressure on the draw solution side becomes higher than the osmotic pressure, onset of the reverse osmosis

* Corresponding author.

process will result, where water permeates from the draw solution side to the feed solution side, that is, from the higher to lower salinity solution [3].

Fig. 1 shows a schematic for a typical PRO process. As shown, the process includes four primary units: the membrane module, the draw solution regeneration unit, a turbine for energy generation, and feed pumps [1,4]. The schematic does not include the pressure exchange unit to pressurize the concentrated draw solution leaving the desalinated water production system. Fig. 2 shows a schematic for the solute concentration profile in two operating modes, where the active layer of the membrane is either facing the draw solution (Fig. 2a) or the feed solution (Fig. 2b). In either operating mode, the water flux flows from the feed to the draw solution side and the salt flux flows in the opposite direction. The optimization of the system is highly dependent on the ratio of the forward water flux to the reverse solute flux, which is a membrane property and is independent of other operating parameters, such as the draw solution concentration, pressures of the draw and feed solutions, or flow rates of the feed and draw solutions [5,6]. In this regard, Philip et al. [6] obtained a closed form expression for the ratio of the water and salt fluxes, which showed that the ratio depends only the membrane selectivity. Further, this relation was proved through comparison of the predictions of this relation against measured data of the membrane selectivity as a function of the draw solution concentration [6].

Our literature review indicates that the modeling of the PRO/FO processes utilize either the solution diffusion (SD) model or the Spiegler–Kedem (SK) model. The SD and SK models become identical as the value of the reflection coefficient used in the SK model approaches unity. However, the

SK model contains three fitting parameters, thereby providing more accurate predictions for the system variables and fits the experimental data better [7]. Another important factor that affects both models is the formation of the concentration polarization layer that reduces the permeation rate of fresh water from the feed solution into the draw solution, and increases the rate solute flux from the draw solution into the feed solution [7–9].

Philip et al. [6] and Benavides and Philip [10] developed a simple analytical model for the PRO/FO process that yielded predictions that match the results obtained by a numerical solution of the governing equations and experimental measurements. Their results and analysis indicated that membrane selectivity and draw solution concentration are the dominant factors that determine the extent of water recovery and solute rejection. Mondal et al. [11] developed an analytical solution for sizing the FO process operating in either co-current or counter-current modes. The model is an integral solution of the mass balance equations. This model provided more accurate predictions than the log mean approximation. More recently, Cheng and Chung [12] derived a set of analytical expressions describing mass transfer for flat sheet membrane as well as single and double skinned hollow fiber membranes. The double skin configuration is developed in order to provide protection against fouling effects of the feed solution.

Nagy [13] and Bui et al. [14] developed detailed resistance in series models of the FO process. The models considered external mass transport resistances in the boundary layer of the feed and draw solutions and within the support layer. Effects of fouling resistance in a similar resistance in series analysis is made by Nagy et al. [15] and expressed the interface concentrations in a closed form. Analysis showed the fouling layer lowers the water flux significantly and the power density.

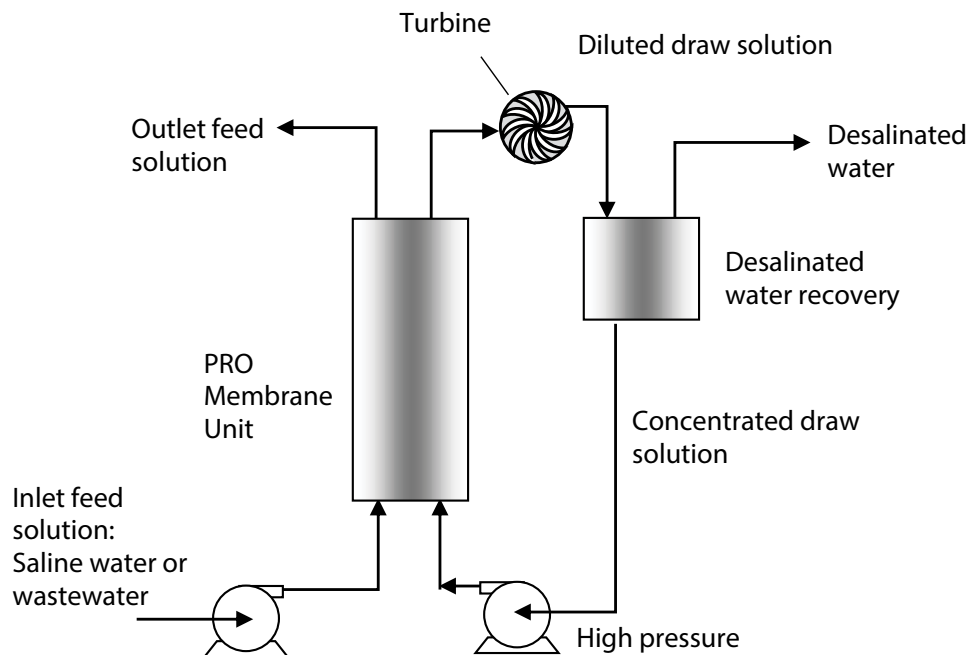


Fig. 1. Schematics of the PRO system.

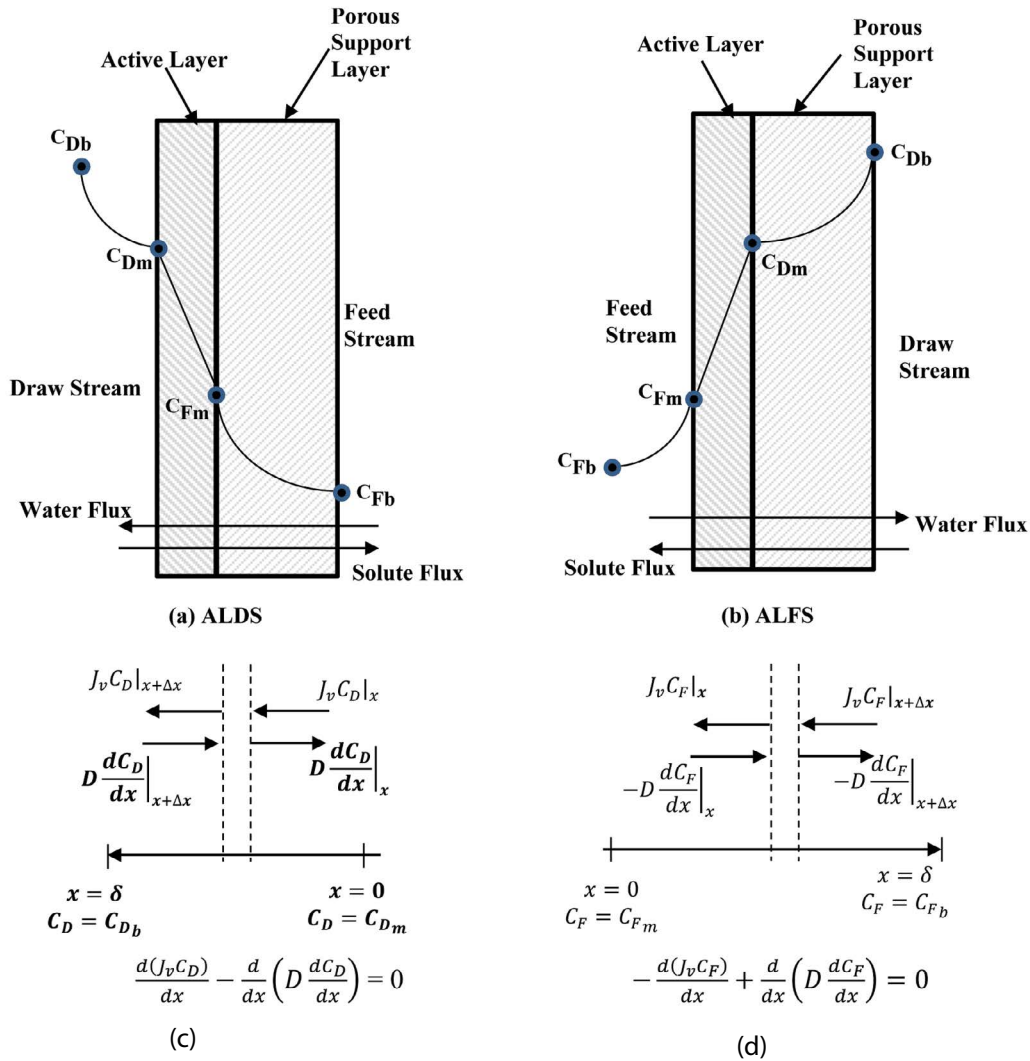


Fig. 2. Schematics of membrane active and support layers, concentration profile, and directions of water and salt fluxes in the modes of (a) active layer facing draw solution (ALDS), (b) active layer facing feed solution (ALFS), (c) differential balance inside the draw solution boundary layer for ALDS, and (d) differential balance inside support layer for ALDS.

Jung et al. [16] showed that an improved FO performance was observed when the draw solution faces the active layer of the membrane. In addition, operating modes that included cross flow, counter-current, and co-current flows of the draw and feed solutions demonstrated no difference in the system performance, including the recovery ratio and permeate flow rate. Meanwhile, the placement of the active layer on the feed side was found necessary for the application of FO with brine reject from an olive factory that was used as the feed solution [17]. This option was chosen because the brine stream contained a high concentration of suspended solids that would have resulted in the fouling and blockage of the support layer. In addition, Xiao et al. [18] concluded that the counter-current module operation provided better internal hydraulic environments. The authors reported that the flow rate ratio of the feed and draw solutions higher than unity would reduce the reverse solute flux from the draw solution to the feed side. A similar study by Ruprakobkit et al. [19] focused on the recovery of various types of carboxylic acids

by FO using 1 M ammonium chloride draw solution. The model was validated against the experimental measurements for several types of carboxylic acids. The model showed the accurate predictions of various performance parameters, and also provided regions of optimal operating conditions.

Xu et al. [20] reported that an increase in the draw solution concentration increased the permeate flow rate; however, an increase in the internal concentration polarization and the dilution of the draw solution near the membrane surface would reduce the permeate flow. They used a simple mathematical model that provided the accurate predictions of the PRO/FO system when the external concentration polarization on the feed side is small. Xue et al. [21] tested plate and frame modules for nutrient concentration in wastewater feed and seawater as a draw solution. In their experiments, the effects of length of membrane module and height of flow channels were tested. The analysis showed that small channel heights are suited for producing concentrated feed, whereas large channel heights are more suited for fresh water

production. In addition, their results indicated that draw solution velocities close to 10 times the feed solution velocity are optimal for operating the plate and frame module in the FO mode.

This study focuses on the modeling and simulation of the PRO/FO processes using the SD and the SK models. The simulation includes two operating configurations, where the membrane active layer faces either the feed solution or the draw solution. In addition, the membrane module is that for the spiral wound configuration and is modeled by the CM or the plug flow (PF) models. Models for the co-current and counter-current flow configurations of the PF system are examined in order to assess findings in previous literature studies that system performance for both flows is similar. The results of the CM and PF models are reported in terms of variations in the recovery ratio, power density, and permeate flow rate as a function of the draw solution concentration and pressure as well as the flow rates of the feed and draw solutions.

2. Mathematical models

This section includes the review of the SD and the SK models, as well as the concentration polarization effects in the membrane support layer and in the fluid boundary layer facing the membrane active layer. In addition, the balance equations are developed for the CM and the PF configurations.

2.1. Solution diffusion model

The solution diffusion model [22] contains two fitting parameters, which are the salt and water permeability. The model equations include a set of four nonlinear equations that maintains the water flux, salt flux, total volume flux, and concentration polarization. The water flux in the PRO mode is proportional to the net driving force for the concentration and pressure differences across the membrane. This relation is given by the equation as follows:

$$J_w = A \left(b \left(C_{D_m} - C_{F_m} \right) - (p_D - p_F) \right) \quad (1)$$

In the FO mode, the pressure difference term in Eq. (1) is zero. The osmotic pressure constant in Eq. (1) is given by the relation:

$$b = \frac{vRT}{M} \quad (2)$$

The salt flux is proportional to the concentration difference between the draw solution side and feed solution side:

$$J_s = -B \left(C_{D_m} - C_{F_m} \right) \quad (3)$$

As shown in Fig. 2, the negative sign of the solute flux implies that the solute flows in the opposite direction to the water flow. The total net flux across the membrane or the hydraulic flux is given in terms of the net sum of the water

and salt fluxes (Eq. (4)). It is noteworthy that the difference between the J_v and J_w is negligible because $J_w \times C_T$ given in Eq. (4) is much larger than the salt flux J_s .

$$J_v = \frac{J_w \times C_T \times J_s}{C_T} \quad (4)$$

The hydraulic flux is also expressed in terms of the concentration polarization constant (ϕ) and the mass transfer coefficient (k) [23]:

$$J_v = -k \ln(\phi) \quad (5)$$

which can be rearranged to

$$\phi = \exp\left(\frac{-J_v}{k}\right) \quad (6)$$

The mass transfer coefficient is obtained from a velocity-based correlation given in [8]:

$$k = 1.1 \times 10^{-4} V^{0.54} \quad (7)$$

The concentration polarization affects the concentration of the feed and draw solutions at the membrane interface. For the case of the active layer facing the draw solution (ALDS), the following relation yields the concentration of the draw solution at the membrane surface [8,23]:

$$C_{D_m} = C_{F_b} + (C_{D_b} - C_{F_b}) \phi_{\text{ALDS}} \quad (8)$$

Eq. (8) is obtained through performing a differential balance inside the draw solution boundary layer next to the active layer of the membrane. As shown in Fig. 2c, the balance includes the diffusion and convective fluxes. For constant diffusion coefficient and volume flux, the resulting equation becomes linear and can be easily integrated to give the result in Eq. (8), which is the same to that reported in the study by Attarde et al. [8]. It should be noted that the first integration constant is assumed equal to $J_v C_{F_b}$. Another form for Eq. (8) which is similar to those reported in the study by Hoek et al. [23] is obtained by setting the integration constant equal to zero.

The concentration of feed solution at the membrane surface is obtained by integrating the solute flux equation across the support layer [8,24]. A schematic for the differential balance within the support layer for the ALDS configuration is shown in Fig. 2d. The resulting equation is given by

$$-J_s = \frac{J_v C_{F_b} \exp(J_v K) - J_v C_{F_m}}{1 - \exp(J_v K)} \quad (9)$$

Eqs. (3) and (9) are combined to eliminate J_s and to obtain an expression for C_{F_m} as a function of J_v , C_{D_m} , C_{F_b} , B , K :

$$C_{F_m} = C_{D_m} \times \frac{B(\exp(J_v K) - 1) + C_{F_b} / C_{D_m} J_v \exp(J_v K)}{B(\exp(J_v K) - 1) + J_v} \quad (10)$$

The concentrations of the feed and draw solutions at the membrane surface for ALFS configuration are obtained using the same procedure used to derive Eqs. (8)–(10). These equations are also similar to those reported in the literature by Attarde et al. [8], Hoek et al. [23], and Lee et al. [24]:

$$C_{F_m} = C_{D_b} - (C_{D_b} - C_{F_b})\phi_{ALFS} \quad (11)$$

$$C_{D_m} = C_{F_m} \times \frac{B(\exp(-J_v K) - 1) - C_{D_b} / C_{F_m} \times J_v \exp(-J_v K)}{B(\exp(-J_v K) - 1) - J_v} \quad (12)$$

2.2. SK model

The SK model [25] contains three fitting parameters: water permeability, salt permeability, and reflection coefficient. The model equations are similar to those of the SD model and include the hydraulic flux:

$$J_v = A(b\sigma(C_{D_m} - C_{F_m}) - (p_D - p_F)) \quad (13)$$

The salt flux from the draw solution to the feed compartment is given by [7]:

$$J_s = -\frac{J_v(1-\sigma)(C_{D_m} - \exp(J_v(1-\sigma)/B)C_{F_m})}{(\exp(J_v(1-\sigma)/B) - 1)} \quad (14)$$

The concentration polarization constant (f) is given by Eq. (6). For the ALDS case, the membrane concentration of draw solution is given by Eq. (8) and the membrane concentration of the feed solution is obtained by similar procedure which is described in the previous section [7].

$$C_{F_m} = C_{D_m} \times \frac{(1 - \exp(J_v(1-\sigma)/B))\exp(J_v K)C_{F_b} / C_{D_b} + (1-\sigma)(1 - \exp(J_v K))}{(1 - \exp(J_v(1-\sigma)/B)) + (1-\sigma)\exp(J_v(1-\sigma)/B)(1 - \exp(J_v K))} \quad (15)$$

Similarly, for the ALFS case, the membrane concentration of feed solution is given by Eq. (11) and the membrane concentration of the draw solution is given by [7]:

$$\frac{C_{D_m}}{C_{F_m}} = \frac{\left[(1 - \exp(J_v(1-\sigma)/B))\exp(-J_v K)C_{D_b} / C_{F_m} - (1-\sigma)\exp(\exp(J_v(1-\sigma)/B))(1 - \exp(-J_v K)) \right]}{(1 - \exp(J_v(1-\sigma)/B)) - (1-\sigma)(1 - \exp(-J_v K))} \quad (16)$$

2.3. Complete mixing model

A schematic for the CM model is shown in Fig. 3a. The model is used to determine the outlet flow rates, concentrations, and pressures from the feed and draw solution compartments. The CM model assumes that the contents of the feed and draw compartments are well mixed and the bulk concentrations are equal to the concentrations of the outlet streams, where $C_{F_b} = C_{F_o}$ and $C_{D_b} = C_{D_o}$. This condition also applies for the CM configuration of the SD and SK models. Therefore, the balance of the total mass and the solute mass

on the draw and feed sides is given by the following set of equations:

$$Q_{F_o} = Q_{F_i} - aJ_v \quad (17)$$

$$Q_{D_o} = Q_{D_i} + aJ_v \quad (18)$$

$$C_{F_o} = \frac{Q_{F_i}C_{F_i} - aJ_s}{Q_{F_o}} \quad (19)$$

$$C_{D_o} = \frac{Q_{D_i}C_{D_i} + aJ_s}{Q_{D_o}} \quad (20)$$

The pressure drop on the feed and draw solution sides is obtained by assuming a constant velocity within each compartment [26]:

$$p_{F_o} = p_{F_i} - f_F \mu \times v_F l_F \quad (21)$$

$$p_{D_o} = p_{D_i} - f_D \mu \times v_D l_D \quad (22)$$

The system recovery ratio is defined as the ratio of the amount of water permeate and the feed stream flow rate:

$$RR = \frac{Q_{D_o} - Q_{D_i}}{Q_{F_i}} \quad (23)$$

The power density of the PRO operating mode is obtained by:

$$W = \frac{(p_{D_o}Q_{D_o} - p_{D_i}Q_{D_i}) - (p_{F_i}Q_{F_i} - p_{F_o}Q_{F_o})}{a} \quad (24)$$

The equations constituting the CM configuration for the SD or SK models were solved using MATLAB (R2017b). The solution of the CM configuration requires solution of Eqs. (1), (3), (5), (8), and (10) for the SD-ALDS system, Eqs. (1), (3), (5), (11), and (12) for SD-ALFS system, Eqs. (5), (8), (13)–(15) for the SK-ALDS system, and Eqs. (5), (13), (14), (11), and (16) for SK-ALFS system. This produces the values of $J_v, J_s, \phi, C_{D_m},$ and C_{F_m} , which is then used to determine the values of $Q_{F_o}, Q_{D_o}, C_{D_o}, C_{F_o}, RR,$ and W from Eqs. (17)–(20), (23), and (24).

2.4. Plug flow model

The PF model assumes a steady-state operation and co-current flow in the feed and draw compartments. The co-current assumption is motivated by the results reported by Jung et al. [16] that indicate negligible differences in the system performance upon changing the flow modes from the co-current to counter-current, or cross flow. Regardless, assessment of the co-current vs. the counter-current operating modes is made because the membrane areas used in this study varied between 0.25 and 0.5 m², while those found in the study by Jung et al. [16] were much smaller with a value of 0.01 m². The counter-current model equations are given in the appendix.

The co-current model schematic is shown in Fig. 3b for a differential membrane area (Δa), which is defined

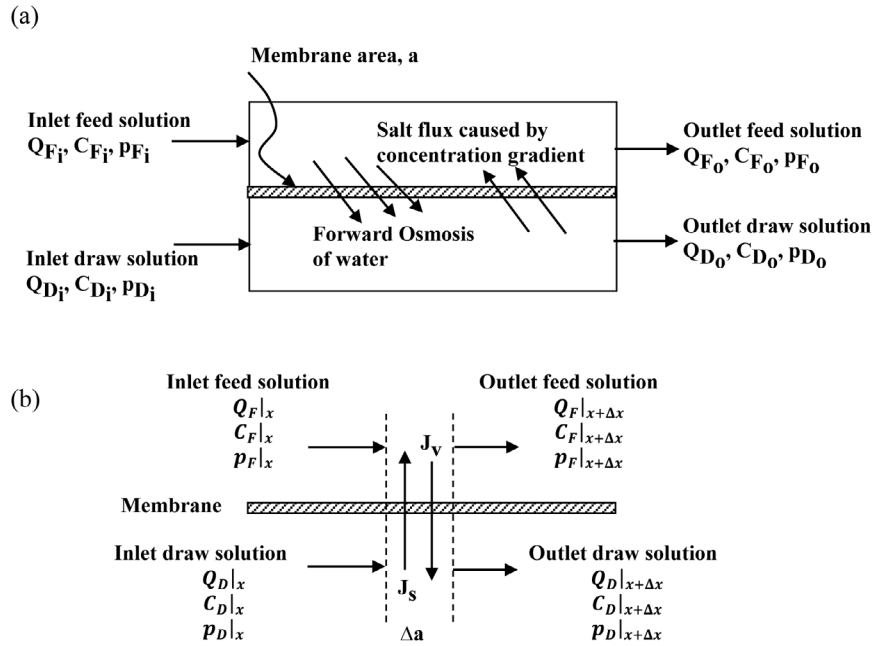


Fig. 3. Schematics of (a) the complete mixing and (b) the co-current plug flow configurations.

by $\Delta a = w \times \Delta x$. The PF model includes six equations that represent the total mass and salt balances and the pressure drop on the feed and draw solution sides. The equations include the following:

$$\frac{dQ_F}{dx} = -2w_F J_v \quad (25)$$

$$\frac{dC_{F_b}}{dx} = \frac{2(-J_s + C_{F_b} J_v)w_F}{Q_F} - \frac{C_{F_b}}{Q_F} \frac{dQ_F}{dx} \quad (26)$$

The pressure drop on the feed side is given by:

$$\frac{dp_F}{dx} = -f_F \mu \frac{Q_F}{h_F w_F} \quad (27)$$

The total mass and salt balance on the draw solution side are given by:

$$\frac{dQ_D}{dx} = 2w_D J_v \quad (28)$$

$$\frac{dC_{D_b}}{dx} = \frac{2(J_s - C_{D_b} J_v)w_D}{Q_D} - \frac{C_{D_b}}{Q_D} \times \frac{dQ_D}{dx} \quad (29)$$

and the pressure drop on the draw solution side

$$\frac{dp_D}{dx} = -f_D \mu \frac{Q_D}{h_D w_D} \quad (30)$$

In Eqs. (26) and (29) and according to Eqs. (3) and (14), the solute flux term J_s has a negative sign and it increases the solute concentration on the feed side and decreases the

solute concentration on the draw solution side. On the other hand, the hydraulic flux J_v has a positive sign, which results in concentrating the feed solution and diluting the draw solution.

It is noteworthy that the power density and recovery ratio for the PF model are identical to Eqs. (23) and (24) given in the CM model. Eqs. (25)–(30) are integrated numerically subject to the following boundary conditions that are defined at the feed and draw solution inlets or at $x = 0$:

$$Q_F = Q_{F_i} \quad (31)$$

$$C_{F_b} = C_{F_i} \quad (32)$$

$$p_F = p_{F_i} \quad (33)$$

$$Q_D = Q_{D_i} \quad (34)$$

$$C_{D_b} = C_{D_i} \quad (35)$$

$$p_D = p_{D_i} \quad (36)$$

The equations constituting the PF configuration for the SD or the SK models were solved using MATLAB (R2017b). The integration of Eqs. (25)–(30) subject to the boundary conditions given by Eqs. (31)–(36) requires the evaluation of the water and salt fluxes, the solution concentrations at the feed and draw sides of the membrane, and the concentration polarization constant. At each integration step and as mentioned at the end of the previous, these variables are obtained from iterative solution of the SD and SK for the ALDS and ALFS configurations.

2.5. Model parameters and operating range

Table 1 shows the ranges and values of parameters and operating conditions used in the simulation. The values of the friction parameters on the feed and draw solution sides are provided by a study by Senthilmurugan et al. [26] for 2.5" and 4" spiral wound reverse osmosis modules. The velocity of the feed and draw solutions depend on the cross-sectional area of the flow channel and the flow rate of each stream. The flow channel area in both the feed and draw solution sides is assumed to be equal to 1.13 m² [17], which yields a velocity varying between 0.012 and 0.05 m/s.

3. Results and discussion

The developed models are compared by calculating the recovery ratio, power density, and permeate flow rate. The calculations are performed as a function of the flow rates, concentrations, and pressures of the feed and draw solutions as well as the membrane area.

Fig. 4 shows the variations in the recovery ratio for the CM configuration, the ALFS and ALDS operating modes, and the SD and SK models, as a function of the flow rates of the feed and draw solutions. The calculations are performed in the FO mode, where the pressures of the feed and draw solutions are maintained at 1 bar. As shown, the recovery ratio decreases with the increasing feed flow rate and decreasing draw solution concentration. The reduction in the recovery ratio occurred because the permeate flow rate

depends primarily on the driving force across the membrane that includes the membrane area, hydraulic pressure difference, and concentration difference. Therefore, the permeate flow changes slightly upon the increasing flow rates of either stream. The results for the ALFS modes (Figs. 4a and b) yield similar values for both SD and SK models with a deviations of less than 3%, which is defined as the ratio of the difference between the predictions of the SD and SK models to the prediction of the SK model. This low difference occurred because the permeation resistance due to the concentration polarization within the membrane support layer is high, and it controls the water and salt fluxes across the membrane.

Examining the results of the ALDS operating mode (Figs. 4c and d) demonstrate higher recovery ratios by both models. Further, the SK model exhibited higher values for the recovery ratio than the SD model. This is due to the reflection coefficient that negates some of the effects of the concentration polarization and causes an increase in the permeate flux, and hence the recovery ratio. This finding is confirmed through examination of the difference of the $C_{D_m} - C_{F_m}$ predicted by the SD and SK models, which controls the permeation flow rate as shown in Eqs. (1) and (13). The data showed that values for C_{D_m} predicted by both models are similar, on the other hand, values for C_{F_m} predicted by the SK model are much lower and as a result the difference of $C_{D_m} - C_{F_m}$ in the SK model is higher by 15%–30% than those of the SD model. Therefore, the SK model in the ALDS operating mode gives higher values for the permeate flow rate and recovery ratio.

Fig. 5 shows the effect of increasing the draw solution concentration on the recovery ratio. As mentioned above, the permeate flow rate across the membrane depends primarily on the differences in the concentration and pressure, as well as the membrane area and the membrane resistance to water and salt transport. Therefore, increasing the draw solution concentration to a value of 60 g/L and maintaining the feed solution concentration constant at 1 g/L provide a large driving force for water flow across the membrane. The results shown in Fig. 5 favor the ALDS operating mode, which yields higher recovery ratios than the ALFS mode. Further, the SK model yields higher recoveries than the SD model. As discussed above, the salt flux in the ALFS mode flows from the draw side through the support layer and subsequently into the membrane. This yields a concentration polarization factor that is larger than that obtained in the ALDS mode; this in turn reduces the water flux across the membrane.

The characteristics of the PRO system are shown in Figs. 6 and 7 as a function of the variations in the power density and permeate flow rate. The calculations are performed by varying the inlet pressure and the concentration of the draw solution. The change in the power density, which is proportional to the permeate flow rate and draw solution pressure, yields a maximum as a function of the draw solution pressure. This is because as the draw solution pressure increases, the permeate flow rate decreases. The increase in the power density occurs because of the dominant effect of the draw solution pressure and the relatively high values of the permeate flow rate. At higher draw solution pressures, the permeate flow rate continues to decline, causing the power density to reach its maximum value. The maximum and highest value of the power density is equal to 2 W/m²

Table 1
Range and value of model parameters and operating conditions

Parameter	Range/value
Membrane area (a)	0.25–0.5 m ²
Width of feed/draw side channel (w_F, w_D)	0.25–0.5 m
Height of feed/draw side channel (h_F, h_D)	0.01 m
Compartment length of the feed/draw side (l_F, l_D)	1 m
Feed solution flow rate (Q_F)	5–22 L/h
Draw solution flow rate (Q_D)	5–17 L/h
Concentration of the feed solution (C_F)	1.5 g/L
Concentration of the draw solution (C_D)	10–60 g/L
Pressure of feed solution (p_F)	0.5 bar
Pressure of draw solution (p_D)	1–40 bar
Inlet concentration of feed solution (C_{F_i})	1 g/L
Inlet concentration of draw solution (C_{D_i})	15–60 g/L
Temperature (T)	25°C
Water permeability (A)	1.8×10^{-12} m/s Pa
Solute permeability (B)	1.6×10^{-7} m/s
Mass transfer coefficient (k)	6×10^{-5} m/s
Solute resistivity (K)	3.88×10^5 s/m
Reflection coefficient (σ)	0.91
Feed/draw solution viscosity (μ)	0.001 s Pa
Friction coefficient on the feed/draw side (f_F, f_D)	2×10^{-8} m ⁻²
Velocity of the feed/draw solution (v_F, v_D)	0.012–0.05 m/s

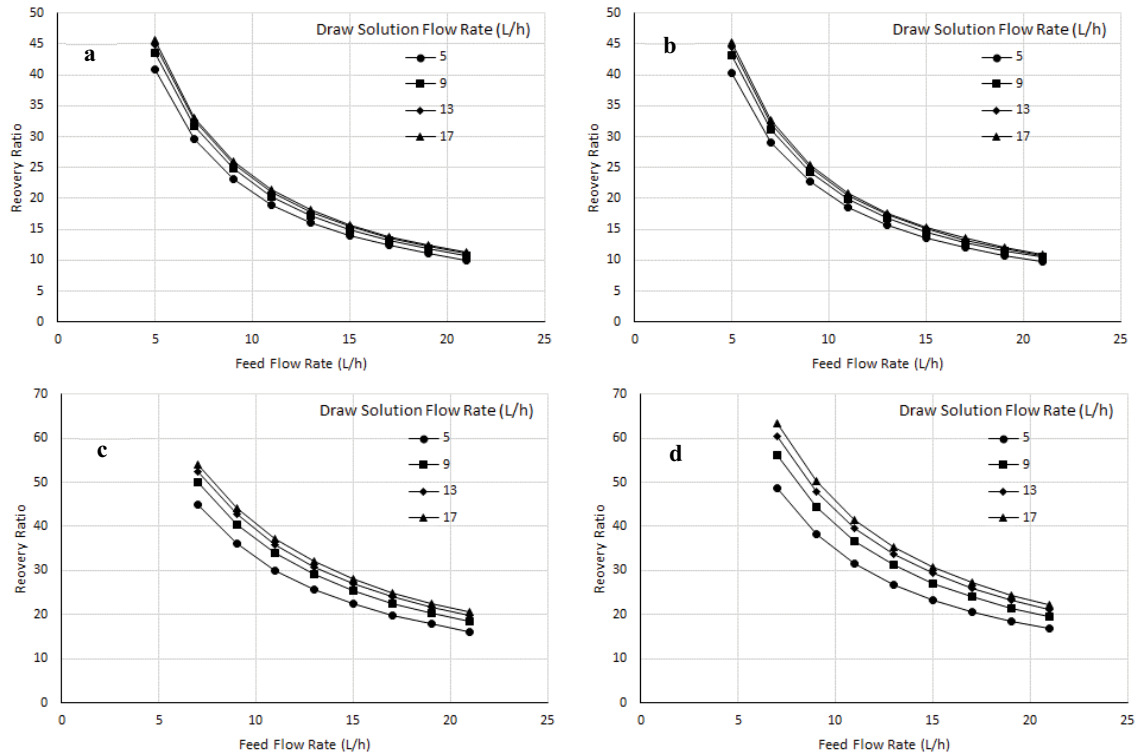


Fig. 4. Variation in the recovery ratio as a function of the feed and draw solution flow rates for the complete mixing configuration, and (a) SD-ALFS, (b) SK-ALFS, (c) SD-ALDS, (d) SK-ALDS. All data are calculated at $p_{F_i} = 1$ bar, $p_{D_i} = 1$ bar, $C_{F_i} = 1$ g/L, $C_{D_i} = 60$ g/h, $a = 0.25$ m².

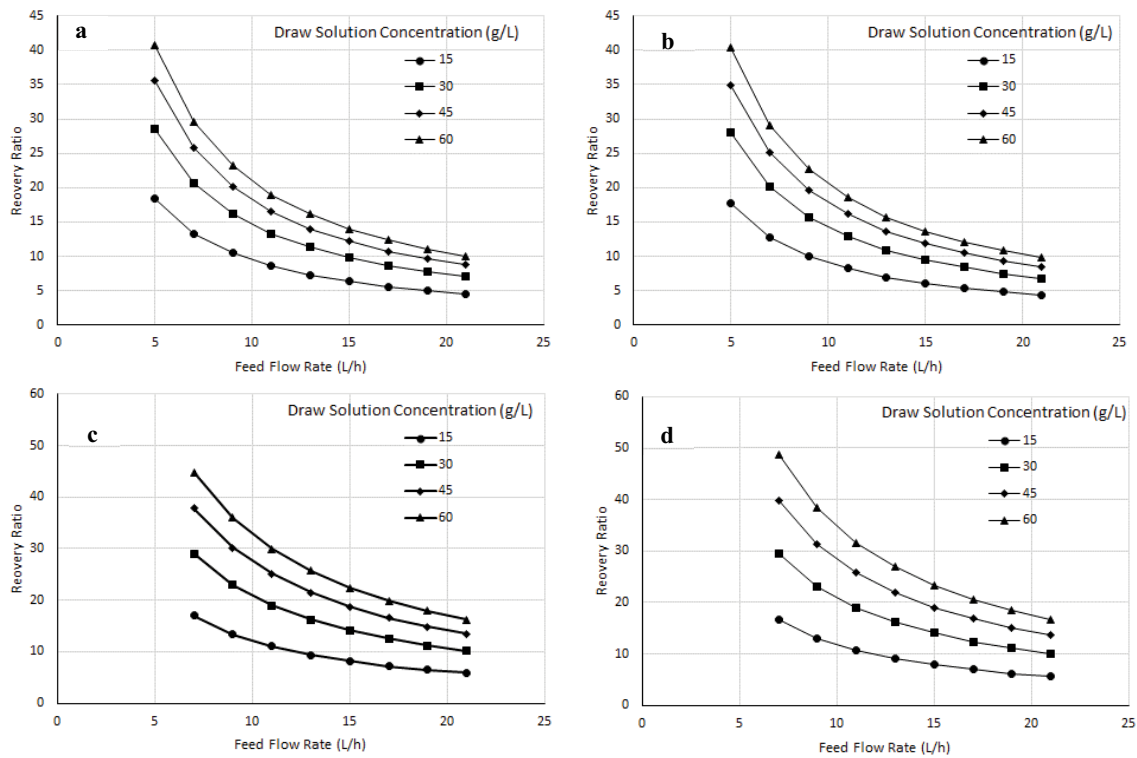


Fig. 5. Variation in the recovery ratio as a function of the feed flow rate and the draw solution concentration for (a) SD-ALFS, (b) SK-ALFS, (c) SD-ALDS, (d) SK-ALDS. All data are calculated at $p_{F_i} = 1$ bar, $p_{D_i} = 1$ bar, $C_{F_i} = 1$ g/L, $Q_{D_i} = 5$ L/h, $a = 0.25$ m².

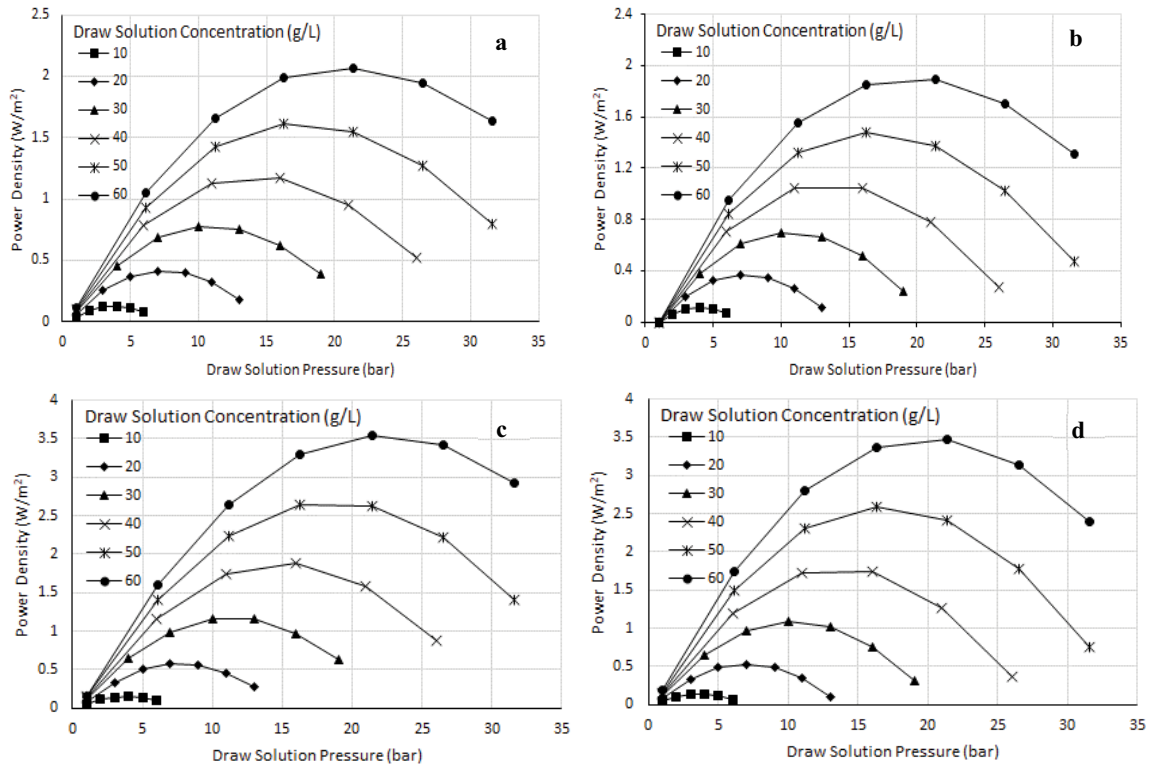


Fig. 6. Variation in the power density as a function of draw solution inlet pressure and inlet concentration for (a) SD-ALFS, (b) SK-ALFS, (c) SD-ALDS, (d) SK-ALDS. All data are calculated at $p_{F_i} = 1$ bar, $C_{F_i} = 1$ g/L, $Q_{F_i} = 5$ L/h, $Q_{D_i} = 5$ L/h, $a = 0.25$ m².

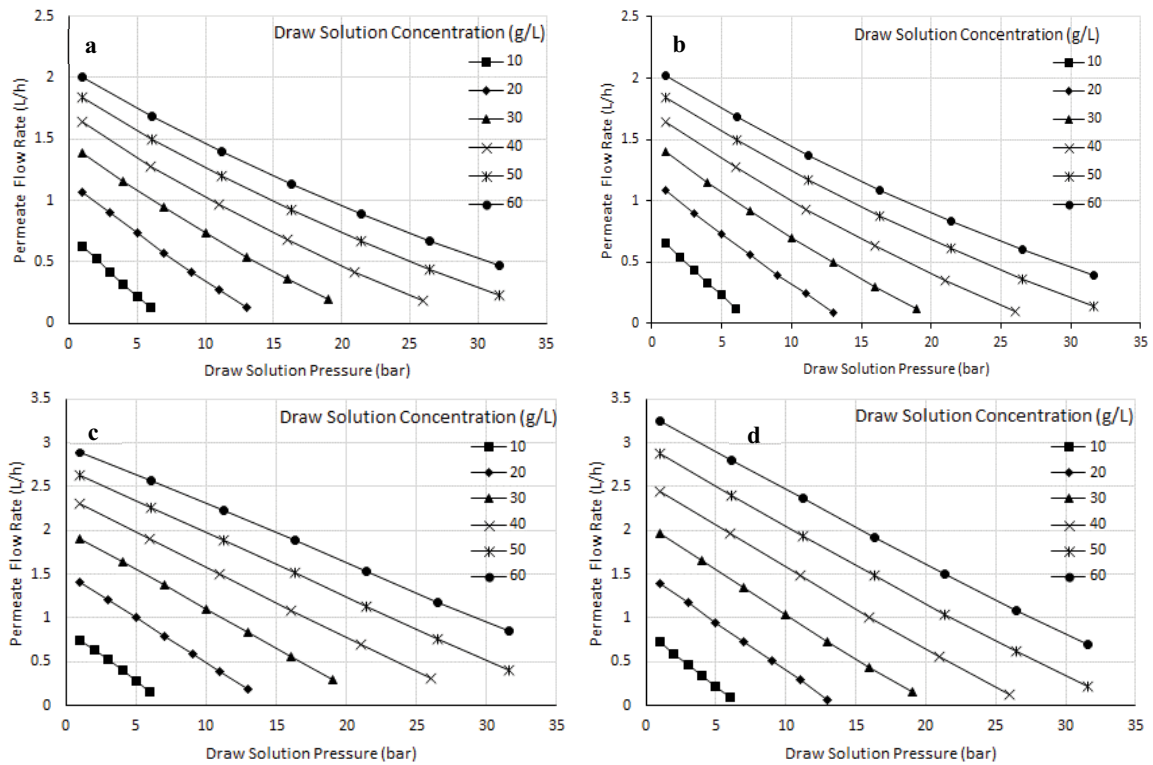


Fig. 7. Variation in the permeate flow rate as a function of the draw solution pressure and concentration for (a) SD-ALFS, (b) SK-ALFS, (c) SD-ALDS, (d) SK-ALDS. All data are calculated at $p_{F_i} = 1$ bar, $C_{F_i} = 1$ g/L, $Q_{F_i} = 5$ L/h, $Q_{D_i} = 5$ L/h, $a = 0.25$ m².

for the ALFS mode, and 3.5 W/m² for the ALDS mode. These values occur at draw solution pressures of 22 bar and draw solution concentration of 60 g/L. It should be noted that this pressure is approximately equal to 50% of the draw solution osmotic pressure, which is consistent with literature data [20]. At this pressure and concentration, the permeate flow rate is equal to 0.8 L/h for the ALFS mode and 1.5 L/h for ALDS mode.

Assessment of the co-current and counter-current assumptions for the PF model is made for a membrane area of 0.35 m², feed flow rates of 14–22 L/h, and draw solution flow rates of 5–13 L/h. Results are given in Fig. 8 for variations in the recovery ratio as a function of the two flow rates. As shown, at higher flow rates of the draw solution, the two flow configurations gave almost identical results. While, at lower flow rates, small deviations between the two models are obtained, which varied between 5% and 7%. In light of these results, it is concluded that the co-current assumption for the PF is valid and is used in the following comparison of the PF and CM models.

A comparison of the PF and CM model predictions for the SD model and the ALDS operating mode are shown in Figs. 9 and 10, respectively. Fig. 9 shows the variations in the recovery ratio as a function of the flow rates of the feed and draw solutions. All calculations were performed for a membrane area of 0.5 m², inlet concentrations of 1 and 60 g/L for the feed and draw solutions, respectively, and equal pressures of 1 bar for the feed and draw solutions. In all cases, the PF model yields higher values for the permeation rate, power density, and permeate flow rate. This is caused by the dilution effects within the feed and draw solution compartments in the CM model that reduces the driving force for permeation, and hence lowers the recovery ratio and power density. Nevertheless, the results predicted by both models exhibit similar trends, and the deviations in the predictions for the two models are less than 11%. The deviation is defined as the difference in the parameter value by the two models to the predictions of the PF model.

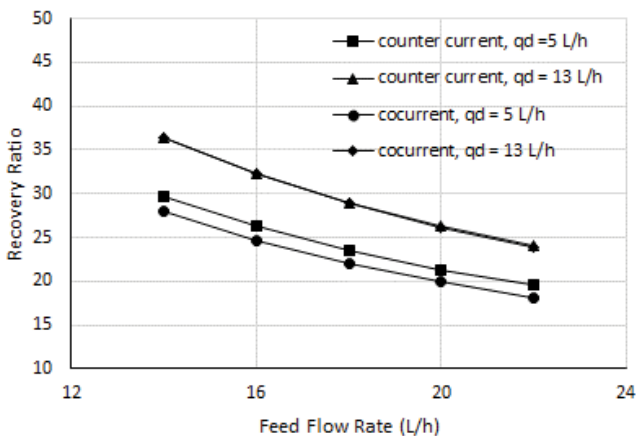


Fig. 8. Variation in the recovery ratio for the FO system as predicted by the co-current and counter-current plug flow (PF) models, and as a function of the flow rates of the inlet feed and draw solutions. All data are calculated at $C_{F_i} = 1$ g/L, $C_{D_i} = 60$ g/L, $p_{F_i} = 1$ bar, $p_{D_i} = 1$ bar, $a = 0.35$ m².

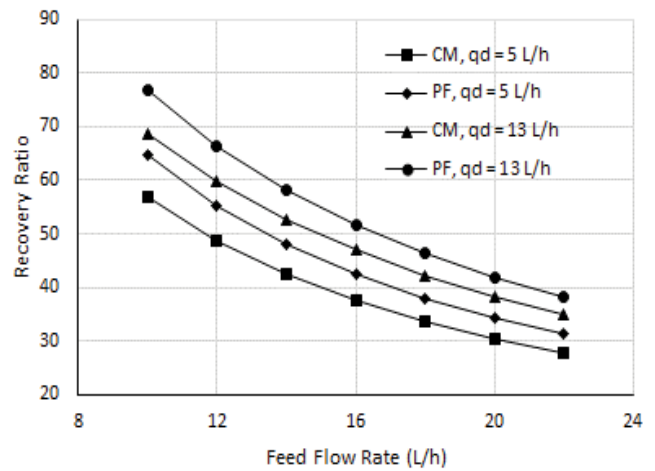


Fig. 9. Variation in the recovery ratio for the FO system as predicted by plug flow (PF) and complete mixing (CM) models, and as a function of the flow rates of the feed and draw solutions. All data are calculated at $C_{F_i} = 1$ g/L, $C_{D_i} = 60$ g/L, $p_{F_i} = 1$ bar, $p_{D_i} = 1$ bar, $a = 0.5$ m².

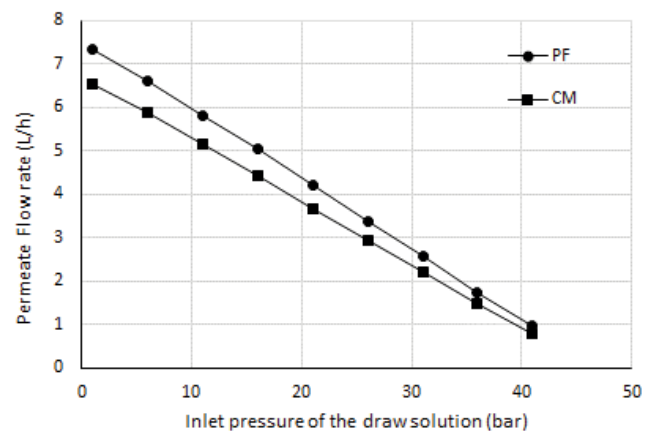
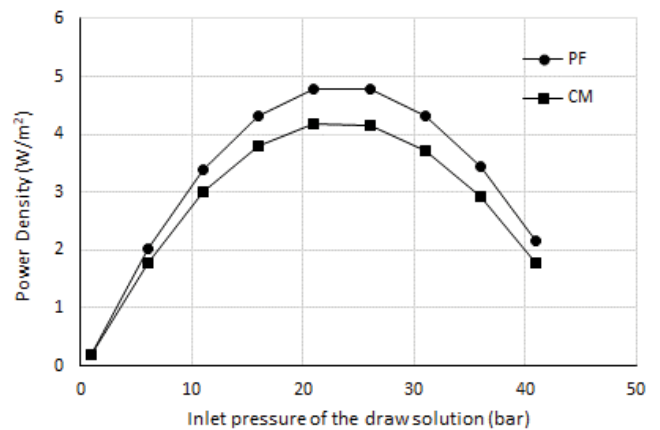


Fig. 10. Variation in the power density and the permeate flow rate for the plug flow (PF) and complete mixing (CM) models, and as a function of the inlet pressure of the draw solution concentration. All data are calculated at $C_{F_i} = 1$ g/L, $C_{D_i} = 60$ g/L, $p_{F_i} = 0.5$ bar, $Q_{F_i} = 10$ L/h, $Q_{D_i} = 10$ L/h, $a = 0.5$ m².

Variations in the power density and permeate flow rate for the PRO system, as shown in Fig. 10, are similar for the PF and CM models. The deviations in the predictions of the two models were less than 15%. The predictions of the power density for the two models at inlet draw pressures of less than 4 bar are almost identical. This is caused by the small pressure difference between the draw and feed sides. At higher pressures for the draw solution, the permeate flow rate also shows slight difference in the predictions of the two models. This is caused by the increased retardation effect. As shown in Fig. 10, the maximum power density for either model is obtained at a pressure of 22 bar. This yields the permeate flow rates of 3.3 L/h for the CM model and 3.6 L/h for the PF model.

4. Conclusions

System analysis was performed as a function of various operating parameters that included the flow rates of the feed and draw solutions, concentration of draw solution, and pressure of draw solution. The analysis demonstrated that the selection of the ALDS operating mode provided higher recovery ratio, permeate flow rate, and power density than the ALFS operating mode. However, the system operation in the ALFS mode might be the more feasible choice when the feed solution contains fouling or scaling material that might penetrate and block the support layer. The deviations between the two operating modes exhibited variations between 15% and 45% for the predictions of the recovery ratio, permeate flow rate, and power density. The difference in predicting the system variables is caused by the larger magnitude of the concentration polarization formed in the support layer facing the draw solution for the ALFS operating mode. Therefore, a lower driving force for permeation and a smaller amount of permeate flow rate passes through the membrane, thereby resulting in the reduction of the recovery ratio and power density. It is noteworthy that neither operating mode is favored, and the selection is dependent on the quality of the feed stream [18,20].

The prediction comparisons between the SD model and SK model demonstrate deviations between 1% and 25% for the system recovery ratio, permeate flow rate, and power density. In this case, the SK model should be favored because literature studies [7,26] reported that the SK model provided better fitting results against experimental data. Nevertheless, it is noteworthy that the system performance predicted by the two models is similar. For example, the optimum pressure of the draw solution in the PRO mode, which yielded the highest power density, was the same for either model.

Comparison of the co-current and counter-current flow modes of the PF system showed small deviations in the predictions of the recovery ratio. However, it should be stressed that in full-scale commercial units, where the membrane areas might reach 40 m², larger deviations in system design or simulation can be experienced.

A similar conclusion was demonstrated for the CM and PF models, where the deviations in predicting the system variables between the two models were less than 15%. Therefore, the simplicity of the CM model might prove to be highly useful in obtaining the preliminary design data and performance analysis results. However, this advantage is highly dependent on the membrane area as well as the flow rates of the feed and draw solutions. The CM model would

fail as the membrane area increases to a commercial scale. As a result, the PF model would provide more accurate system data and should yield better results for the fitting parameters, such as the salt and water permeability coefficients and the reflection coefficient.

Symbols

a	—	Membrane area, m ²
A	—	Water permeability, m/s Pa
b	—	Osmotic pressure constant, Pa/(g/L)
B	—	Salt permeability, m/s
C	—	Solute concentration, g/L
C_T	—	Total concentration or density, g/L
f	—	Friction parameter, 1/m ²
h	—	Height of spiral wound channel, m
J_w	—	Water flux, m/s
J_s	—	Solute flux, kg/m ² s
J_v	—	Hydraulic flux, m/s
k	—	Mass transfer coefficient, m/s
K	—	Solute resistivity, s/m
l	—	Membrane length, m
M	—	Molecular weight, g/mole
p	—	Pressure, Pa
Q	—	Flow rate, m ³ /s
R	—	Universal gas constant, m ³ Pa/mole K
RR	—	Recovery ratio, dimensionless
T	—	Temperature, K
V	—	Stream velocity, m/s
w	—	Width of spiral wound flow channel, m
W	—	Power density, W/m ²
x	—	Differential length along the membrane length
ALDS	—	Active layer facing draw solution
ALFS	—	Active layer facing feed solution
CM	—	Complete mixing model
PRO	—	Pressure retarded osmosis
PF	—	Plug flow model
SD	—	Solution diffusion model
SK	—	Spiegler–Kedem model

Greek

μ	—	Dynamics viscosity, Pa s
σ	—	Reflection coefficient, dimensionless
ν	—	Solute valency
φ	—	Concentration polarization constant

Subscripts

b	—	Bulk side
D	—	Draw solution
F	—	Feed solution
i	—	Inlet stream
m	—	Membrane side
o	—	Outlet stream
p	—	Permeate

References

- [1] J.R. McCutcheon, R.L. McGinnis, M. Elimelech, A novel ammonia-carbon dioxide forward (direct) osmosis desalination process, *Desalination*, 174 (2005) 1–11.

- [2] R.L. McGinnis, N.T. Hancock, M.S. Nowosielski-Slepowron, G.D. McGurgan, Pilot demonstration of the NH_3/CO_2 forward osmosis desalination process on high salinity brines, *Desalination*, 312 (2010) 67–74.
- [3] T.Y. Cath, A.E. Childress, M. Elimelech, Forward osmosis: principles, applications, and recent developments, *J. Membr. Sci.*, 281 (2006) 70–78.
- [4] Y. Yang, M. Chen, S. Zou, X. Yang, T.E. Long, Z. He, Efficient recovery of polyelectrolyte draw solutes in forward osmosis towards sustainable water treatment, *Desalination*, 422 (2017) 134–141.
- [5] T.S. Chung, S. Zhang, K.Y. Wang, J. Su, M.M. Ling, Forward osmosis processes: yesterday, today and tomorrow, *Desalination*, 287 (2012) 78–81.
- [6] W.A. Philip, J.S. Yong, M. Elimelech, Reverse draw solute permeation in forward osmosis: modeling and experiments, *Environ. Sci. Technol.*, 44 (2010) 5170–5176.
- [7] D. Attarde, M. Jain, S.K. Gupta, Modeling of a forward osmosis and a pressure-retarded osmosis spiral wound module using the Spiegler-Kedem model and experimental validation, *Sep. Purif. Technol.*, 164 (2016) 182–197.
- [8] D. Attarde, M. Jain, K. Chaudhary, S.K. Gupta, Osmotically driven membrane processes by using a spiral wound module – modeling, experimentation and numerical parameter estimation, *Desalination*, 361 (2015) 81–94.
- [9] J.R. McCutcheon, M. Elimelech, Influence of concentrative and dilutive internal concentration polarization on flux behavior in forward osmosis, *J. Membr. Sci.*, 284 (2006) 237–247.
- [10] S. Benavides, W.A. Phillip, Water recovery and solute rejection in forward osmosis modules: modeling and bench-scale experiments, *J. Membr. Sci.*, 505 (2016) 26–35.
- [11] S. Mondal, R.W. Field, J.J. Wu, Novel approach for sizing forward osmosis membrane systems, *J. Membr. Sci.*, 541 (2012) 321–328.
- [12] Z.L. Cheng, T.S. Chung, Mass transport of various membrane configurations in pressure retarded osmosis (PRO), *J. Membr. Sci.*, 537 (2017) 160–176.
- [13] E. Nagy, A general, resistance-in-series, salt- and water flux models for forward osmosis and pressure-retarded osmosis for energy generation, *J. Membr. Sci.*, 460 (2014) 71–81.
- [14] N.N. Bui, J.T. Arena, J.R. McCutcheon, Proper accounting of mass transfer resistances in forward osmosis: improving the accuracy of model predictions of structural parameter, *J. Membr. Sci.*, 492 (2015) 289–302.
- [15] E. Nagy, I. Hegedüs, E.W. Tow, J.H. Lienhard V, Effect of fouling on performance of pressure retarded osmosis (PRO) and forward osmosis (FO), *J. Membr. Sci.*, 565 (2018) 450–492.
- [16] D.H. Jung, J. Lee, D.Y. Kim, Y.G. Lee, M. Park, S. Lee, D.R. Yang, J.H. Kim, Simulation of forward osmosis membrane process: effect of membrane orientation and flow direction of feed and draw solutions, *Desalination*, 277 (2012) 83–91.
- [17] M.R.S. Sousa, J. Lora-Garcia, M.F. López-Pérez, Experimental study and modeling of forward osmosis process for activated sludge concentration by using residual brine from a stuffed olive factory as draw solution, *J. Water Process Eng.*, 21 (2018) 143–153.
- [18] D. Xiao, W. Li, S. Chou, R. Wang, C.Y. Tang, A modeling investigation on optimizing the design of forward osmosis hollow fiber modules, *J. Membr. Sci.*, 392–393 (2012) 76–87.
- [19] T. Ruprakobkit, L. Ruprakobkit, C. Ratanatamskul, Carboxylic acid concentration by forward osmosis processes: dynamic modeling, experimental validation and simulation, *Chem. Eng. J.*, 306 (2016) 538–549.
- [20] Y. Xu, X. Peng, C.Y. Tang, Q.S. Fu, S. Nie, Effect of draw solution concentration and operating conditions on forward osmosis and pressure retarded osmosis performance in a spiral wound module, *J. Membr. Sci.*, 348 (2010) 298–309.
- [21] W. Xue, K. Yamamoto, T. Tobino, C. Ratanatamskul, Modeling prediction of the process performance of seawater-driven forward osmosis for nutrients enrichment: Implication for membrane module design and system operation, *J. Membr. Sci.*, 515 (2016) 7–21.
- [22] J.G. Wijmans, R.W. Baker, The solution-diffusion model: a review, *J. Membr. Sci.*, 107 (1995) 1–21.
- [23] E.M.V. Hoek, A.S. Kim, M. Elimelech, Influence of crossflow membrane filter geometry and shear rate on colloidal fouling in reverse osmosis and nanofiltration separations, *Environ. Eng. Sci.*, 19 (2002) 357–372.
- [24] K.L. Lee, R.W. Baker, H.K. Lonsdale, Membranes for power generation by pressure retarded osmosis, *J. Membr. Sci.*, 8 (1981) 141–171.
- [25] K.S. Spiegler, O. Kedem, Thermodynamics of hyperfiltration (reverse osmosis): criteria for efficient membranes, *Desalination*, 1 (1966) 311–326.
- [26] S. Senthilmurugan, A. Ahluwalia, S.K. Gupta, Modeling of a spiral-wound module and estimation of model parameters using numerical techniques, *Desalination*, 173 (2005) 269–286.

Appendix A:

Counter-current PF model

The schematic of the counter-current PF model is shown in Fig. A1. The model equations are derived for a differential membrane area (Δa), which is defined by $\Delta a = w \times \Delta x$. The equations include the following:

$$\frac{dQ_F}{dx} = -2w_f J_v \quad (\text{A.1})$$

$$\frac{dC_{F_b}}{dx} = \frac{2(-J_s + C_{F_b} J_v) h_F}{Q_F} - \frac{C_{F_b}}{Q_F} \times \frac{dQ_F}{dx} \quad (\text{A.2})$$

The pressure drop on the feed side is given by:

$$\frac{dp_F}{dx} = -f_F \mu \frac{Q_F}{h_f w_F} \quad (\text{A.3})$$

The total mass and salt balance on the draw solution side are given by:

$$\frac{dQ_D}{dx} = -2w_D J_v \quad (\text{A.4})$$

$$\frac{dC_{D_b}}{dx} = \frac{2(-J_s + C_{D_b} J_v) h_D}{Q_D} - \frac{C_{D_b}}{Q_D} \times \frac{dQ_D}{dx} \quad (\text{A.5})$$

and the pressure drop on the draw solution side is given by:

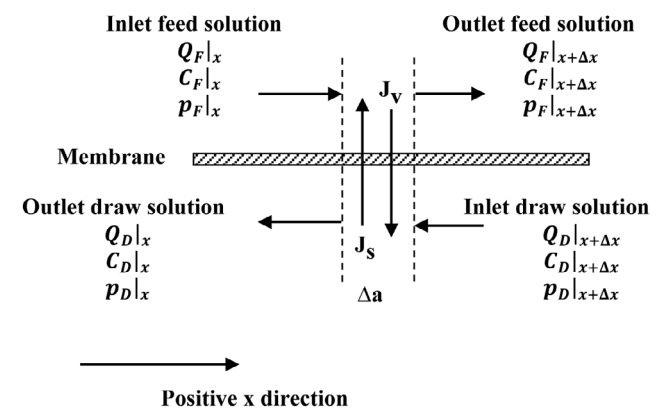


Fig. A1. Schematics of counter-current plug flow configuration.

$$\frac{dp_D}{dx} = -f_D \mu \frac{Q_D}{h_D w_D} \tag{A.6}$$

In Eqs. (A.1) and (A.4), the negative sign on the right side implies decrease of the flow rates on the feed and draw sides along the positive x-direction. This behavior is shown in Fig. A1 for variations in the flow rates of the feed and draw solution along the membrane area.

In Eqs. (A.2) and (A.5) and according to Eqs. (3) and (14), the solute flux term J_s has a net positive sign and it causes increase of the solute concentration on both sides of the membrane. A similar effect is experienced by the hydraulic flux J_v which has a positive sign and results in concentrating the feed solution as well as the draw solution.

Eqs. (A.1)–(A.6) are integrated numerically subject to the following boundary conditions that are defined at the feed and draw solution inlets or at $x = 0$:

$$Q_F = Q_{F_i} \tag{A.7}$$

$$C_{F_b} = C_{F_i} \tag{A.8}$$

$$p_F = p_{F_i} \tag{A.9}$$

$$Q_D = Q_{D_o} \tag{A.10}$$

$$C_{D_b} = C_{D_o} \tag{A.11}$$

$$p_D = p_{D_o} \tag{A.12}$$

It should be noted that the values of Q_{D_o} , C_{D_o} , p_{D_o} are not known; however, the values of Q_{D_i} , C_{D_i} , p_{D_i} at $x = l$ are known. Therefore, the solution is iterative and is made by guessing the values of Q_{D_o} , C_{D_o} , p_{D_o} . The exact solution is obtained

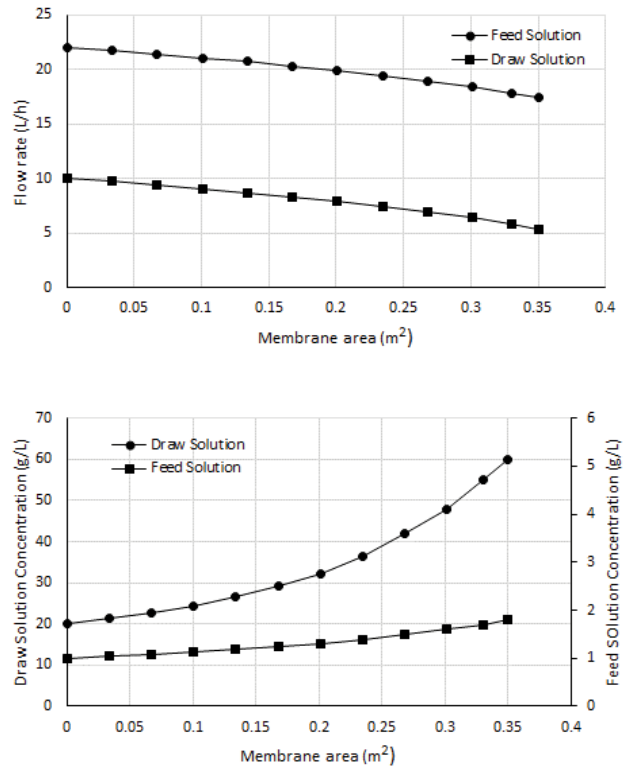


Fig. A2. Flow rates and concentration profiles for the counter-current PF model. All data are calculated at $Q_{F_i} = 22$ L/h, $Q_{D_i} = 5.3$ L/h, $C_{F_i} = 1$ g/L, $C_{D_i} = 60$ g/L, $p_{F_i} = 1$ bar, $p_{D_i} = 1$ bar, $a = 0.35$ m².

through interpolation of calculated data at $x = l$ against the desired values. Sample result for the PF configuration is shown in Fig. A2.